



<b>Publication Year</b>	2020
<b>Acceptance in OA @INAF</b>	2022-09-19T14:19:51Z
<b>Title</b>	Variability and transient search in the SUDARE-VOICE field: a new method to extract the light curves
<b>Authors</b>	Liu, Dezi; Deng, Wenqiang; Fan, Zuhui; Fu, Liping; COVONE, GIOVANNI; et al.
<b>DOI</b>	10.1093/mnras/staa558
<b>Handle</b>	<a href="http://hdl.handle.net/20.500.12386/32605">http://hdl.handle.net/20.500.12386/32605</a>
<b>Journal</b>	MONTHLY NOTICES OF THE ROYAL ASTRONOMICAL SOCIETY
<b>Number</b>	493

# Variability and transient search in the SUDARE-VOICE field: a new method to extract the light curves

Dezi Liu<sup>1,2\*</sup>, Wenqiang Deng<sup>1,3</sup>, Zuhui Fan<sup>1†</sup>, Liping Fu<sup>2‡</sup>, Giovanni Covone<sup>4,5,6</sup>,  
Mattia Vaccari<sup>7,8</sup>, Mario Radovich<sup>9</sup>, Massimo Capaccioli<sup>5</sup>, Demetra De Cicco<sup>10,11</sup>,  
Aniello Grado<sup>4</sup>, Lucia Marchetti<sup>12,7,8</sup>, Nicola Napolitano<sup>4</sup>, Maurizio Paolillo<sup>5,4,6</sup>,  
Giuliano Pignata<sup>13,10</sup>, Fabio Ragosta<sup>5,4,6</sup>

<sup>1</sup>South-Western Institute for Astronomy Research, Yunnan University, Kunming 650500, China

<sup>2</sup>The Shanghai Key Lab for Astrophysics, Shanghai Normal University, 100 Guilin Road, Shanghai 200234, China

<sup>3</sup>School of Physics and Astronomy, Yunnan University, Kunming 650500, China

<sup>4</sup>INAF–Osservatorio Astronomico di Capodimonte, Salita Moiariello 16, Napoli 80131, Italy

<sup>5</sup>Department of Physics, University of Napoli Federico II, via Cinthia 9, 80126 Napoli, Italy

<sup>6</sup>INFN, Sezione di Napoli, Napoli 80126, Italy

<sup>7</sup>Department of Physics & Astronomy, University of the Western Cape, Robert Sobukwe Road, 7535 Bellville, Cape Town, South Africa

<sup>8</sup>INAF - Istituto di Radioastronomia, via Gobetti 101, 40129 Bologna, Italy

<sup>9</sup>INAF–Osservatorio Astronomico di Padova, vicolo dell’Osservatorio 5, Padova 35122, Italy

<sup>10</sup>Millennium Institute of Astrophysics (MAS), Nuncio Monseñor Sotero Sanz 100, Providencia, Santiago, Chile

<sup>11</sup>Instituto de Astrofísica, Pontificia Universidad Católica de Chile, Av. Vicuña Mackenna 4860, 7820436 Macul, Santiago, Chile

<sup>12</sup>Department of Astronomy, University of Cape Town, Private Bag X3, Rondebosch 7701, Cape Town, South Africa

<sup>13</sup>Departemento de Ciencias Físicas, Universidad Andres Bello, Avda. Republica 252, Santiago, Chile

Accepted XXX. Received YYY; in original form ZZZ

## ABSTRACT

The VST Optical Imaging of the CDFS and ES1 Fields (VOICE) Survey, in synergy with the SUDARE survey, is a deep optical *ugri* imaging of the CDFS and ES1 fields using the VLT Survey Telescope (VST). The observations for the CDFS field comprise about 4.38 deg<sup>2</sup> down to  $r \sim 26$  mag. The total on-sky time spans over four years in this field, distributed over four adjacent sub-fields. In this paper, we use the multi-epoch *r*-band imaging data to measure the variability of the detected objects and search for transients. We perform careful astrometric and photometric calibrations and point spread function (PSF) modeling. A new method, referring to as differential running-average photometry, is proposed to measure the light curves of the detected objects. With the method, the difference of PSFs between different epochs can be reduced, and the background fluctuations are also suppressed. Detailed uncertainty analysis and detrending corrections on the light curves are performed. We visually inspect the light curves to select variable objects, and present some objects with interesting light curves. Further investigation of these objects in combination with multi-band data will be presented in our forthcoming paper.

**Key words:** methods: data analysis – methods: observational – techniques: image processing – techniques: photometric – catalogs – surveys

## 1 INTRODUCTION

Time-domain astronomy opens a new window to study the properties of astronomical objects. Properly timed observations allow to obtain their light curves which represent the flux variations as

a function of time. The shapes of light curves contain physical information of different types of objects, such as the pulsating stars, active galactic nuclei (AGNs), supernovae (SNe), tidal disruption events (TDEs), and so forth (Strubbe & Quataert 2009; Covone et al. 2000; Wang & Han 2012; Catelan, & Smith 2015; Lawrence 2016). In addition to providing clues on the nature and origin of these variable objects, they can also be used as tools for astrophysical applications. For example, the period-luminosity relations of Cepheids and RR Lyrae stars are crucial anchors in distance mea-

\* E-mail: adzliu@ynu.edu.cn

† E-mail: zuhuifan@ynu.edu.cn

‡ E-mail: fuliping@shnu.edu.cn

surements (Benedict et al. 2007; Rich et al. 2018). The characteristic light-curve behaviors of Type Ia supernovae make them standardizable candles to measure distance on cosmological scales, and thus to probe the expansion history of the Universe (Riess et al. 1998; Perlmutter et al. 1999; Abbott et al. 2019). The brightness drop of stars caused by their transiting planets leads to abundant discoveries of exoplanet candidates (Thompson et al. 2018; Stassun et al. 2018). Given the importance, many surveys have been dedicated to time-domain observations, e.g. the Panoramic Survey Telescope and Rapid Response System (Pan-STARRS; Kaiser (2004)), the Catalina Real-Time Surveys (CRTS; Drake et al. (2009)), the Palomar Transient Factory (PTF/iPTF; Law et al. (2009)), the High Cadence Transient Survey (HiTS; Förster et al. (2016); Martínez-Palomera et al. (2018)), the SkyMapper Transient Survey (Scalzo et al. 2017), and the Zwicky Transient Facility (ZTF; Graham et al. (2019)). The upcoming facilities, such as the Large Synoptic Survey Telescope (LSST; Ivezić et al. (2019)), will also conduct time-domain observations with about a half sky coverage to faint magnitudes.

To identify the variable objects and measure their light curves, different methods have been applied, including the difference imaging analysis (Alard & Lupton 1998; Oelkers et al. 2015; Zackay et al. 2016), and point spread function (PSF) homogenization (Sánchez et al. 2017) *etc.* The forward modeling of the entire image (galaxy+transient) in a non-parametric manner (Fabbro 2001; Astier et al. 2006) has also been applied to obtain high precision light curves for known transients without involving explicit image subtractions. Since its first application to microlensing surveys (Alard & Lupton 1998), the difference imaging (or image subtraction) method has been widely used in many surveys, such as PTF/iPTF, HiTS and ZTF. To perform image subtraction, a reference image should be first built which can either be the image with the best seeing or the coadded image from multiple exposures. A newly observed image is then subtracted from the reference one after PSF homogenization so that the flux variations of the objects therein can be detected from the residual image. The implementation of the image subtraction method is relatively easy and fast. This makes it particularly well suited to search for transients in wide sky surveys. In practice, however, this method suffers from several limitations. Firstly, the PSF varies spatially over the entire image. For telescopes with a large field of view, the PSF variations are generally significant from the center to the edge in the focal plane. Therefore, accurately modeling the PSF and performing homogenization between the reference and new image are challenging. Secondly, the variable background noise between different exposures makes the observed depths different. The subtraction between the reference and new image will further magnify the background noise. The two facts can lead to large uncertainties of the measured variability or even spurious detections (Zackay et al. 2016).

In this paper, we propose a new method, referring to as differential running-average photometry (drap), to measure the variability of objects and apply it to the SUDARE-VOICE *r*-band imaging data by taking the advantage of the long time baseline and high image quality of the survey. This method can moderately mitigate the difference of PSFs between different exposures, and suppress the background fluctuations, making it applicable to data with relatively long time accumulations and a large enough number of exposures. The paper is organized as follows. In section 2, we describe the SUDARE-VOICE observations and detailed data reduction methods. The methodology for light curve extraction is presented in section 3. We show some typical results in section 4. Fi-

nally, summaries are given in section 5. In Appendix A, we explain the PSF variations in drap. All magnitudes quoted in this paper are in the AB system.

## 2 THE SUDARE-VOICE SURVEY

The VOICE survey<sup>1</sup> (PIs: Giovanni Covone & Mattia Vaccari; Vaccari et al. (2016)), in synergy with the SUDARE survey (Cappellaro et al. 2015; Botticella et al. 2017), was proposed to cover about eight square degrees evenly split between the CDFS (Giacconi et al. 2001; Tozzi et al. 2001) and the ES1 (Oliver et al. 2000; Rowan-Robinson et al. 2004; Vaccari et al. 2005) fields in four optical *ugri* bands using VST/OmegaCam camera. The project also includes additional coverage of the COSMOS field (PI: Giuliano Pignata) with a smaller sky coverage but extended to longer baseline of 3 years (De Cicco et al. 2015, 2019). The VST, located at Cerro Paranal, Chile, is a 2.6-m modified Ritchey-Chretien alt-az telescope designed for wide-field optical imaging. The equipped OmegaCAM (Kuijken 2011) is a mosaic of  $8 \times 4$  CCD chips, each with  $4k \times 2k$  pixels. It covers  $1^\circ \times 1^\circ$  field-of-view with a pixel scale of  $0.214''$ .

The SUDARE-VOICE survey aims at providing deep optical images in the targeted fields to enable various astrophysical studies in conjunction with other existing data covering different wavelengths (Vaccari 2015, 2016b; Vaccari et al. 2010). The imaging observations of the CDFS field have been completed. The entire field was divided into four tiles (CDFS1–4), with each about one square degree. Over one hundred exposures, spanning almost two years, with a single exposure time of 360 seconds, were obtained for each tile (Falocco et al. 2015). Observations were performed in dithering mode, made of at least five consecutive exposures in one night (or one epoch), to cover the detector gaps. The images were preprocessed (including instrumental effect removal, flat fielding, CCD gain harmonization, and illumination correction etc.) with the VST-Tube pipeline (Grado et al. 2012). With the multi-epoch imaging data, many astrophysical topics have been investigated, such as the studies of the SN explosion rate (Cappellaro et al. 2015; Botticella et al. 2017), the variability-based selections of AGNs (Falocco et al. 2015; Poulain et al. 2020), as well as the weak gravitational lensing shear measurements and cosmological analyses (Fu et al. 2018; Liu et al. 2018).

The *r*-band observations were taken with a cadence (i.e. the time interval between two consecutive epochs) of about 3–4 days, avoiding the ten days around the full moon. The *g*- and *i*-band observations were taken every seven days, and the *u*-band observations did not have a specific cadence. Because of their best cadence and image quality, we focus on the analyses of *r*-band data in the present study. Totally, there are 35, 25, 34, and 30 epochs for CDFS1–4 fields, respectively. The average  $5\sigma$  limiting magnitude of individual epochs is about 24.3 mag for point source within 1.0 arcsec aperture radius. In the rest of this section, we will give detailed description on the image processing procedures.

### 2.1 Image Reduction

As mentioned above, the *r*-band single exposure images have been preprocessed by the VST-Tube pipeline (Grado et al. 2012). For accurate variability analyses, we start with the images after removing the instrumental effects by the VST-Tube pipeline, and continue to

<sup>1</sup> <http://www.mattiavaccari.net/voice/>

perform additional calibrations by using our customized routines, including cosmic-ray removal, background subtraction, astrometric and photometric calibrations.

### 2.1.1 Cosmic Ray Removal and Background Subtraction

Careful removal of the cosmic rays is crucial because any residuals on the detected astronomical objects may lead to spurious variabilities. We use a modified Python code<sup>2</sup> that implements the L.A. Cosmic algorithm to detect and remove cosmic rays. The algorithm is based on a variant of Laplacian edge detection (van Dokkum 2001). It is capable of detecting and rejecting cosmic rays with arbitrary shape by convolving a 2D Laplacian kernel which is sensitive to variations on small scales. By applying this algorithm, however, we find that the peak values of some unsaturated bright point objects (typically, about ~10-20 such point objects on each CCD chip) can be misclassified as cosmic rays, especially those observed under good seeing conditions. Our analysis shows that their peak values are systematically larger than half of the saturation level of the CCD chips. To overcome the problem, we slightly modify the code to include additional information from a flag map. To create the flag map, we first run SExtractor (version 2.19.5; Bertin & Arnouts (1996)) on each exposure for object detection, and then assign the isophotal pixels of the point objects with peak values larger than half of the saturation level to zero. Other pixels in the flag map are set to be one. With this map, the bright point objects will not be considered for cosmic ray detections. We determine the best parameters by visual inspection of the mask images, and remove the cosmic rays through iterating the algorithm three times. Residual cosmic rays, including those potentially superposing on the bright point objects, will be further rejected in our following reduction procedures.

We run SExtractor to subtract the background for each CCD chip separately. To construct the background map, SExtractor estimates the local background in each mesh of a grid (64×64 pixels) that covers the entire CCD chip. In the presence of bright or saturated stars, however, the local background will be overestimated, hence leading to an underestimate of the fluxes of real objects. Therefore, we perform the background subtraction in two steps. We first create a preliminary background-subtracted image with SExtractor and detect the objects using a low detection threshold (i.e. DETECT\_THRESH=1.5). Then these objects are masked from the original image. To reduce the effect of the residual light which is below the detection threshold, the mask region of each object is slightly enlarged. Using the same method as described in Liu et al. (2017), for a specific object-masked region, the median value  $a$  and variance  $\sigma^2$  are calculated through its adjacent pixels (at least 900 unmasked pixels). The masked pixels are then filled with random numbers sampled by the Gaussian distribution  $N(a, \sigma^2)$ . Compared to the conventional interpolation method, this procedure preserves the local statistical properties and eliminates many artificial effects. Secondly, we re-run SExtractor on the object-masked image to construct the background map and subtract it from the original image. Our analyses show that this method can produce better local background estimate.

<sup>2</sup> <http://www.astro.yale.edu/dokkum/lacosmic/>

### 2.1.2 Astrometric and Photometric Calibrations

We use SCAMP (version 2.2.6; Bertin (2006)) for astrometric and photometric calibrations. The calibrations are performed on every epoch individually. For astrometric calibration, the *Gaia* DR1 catalog (Gaia Collaboration et al. 2016) is used as reference. The final rms offsets of the astrometry are less than 0.06 arcsec along both right ascension and declination axes.

Homogeneous photometric calibration between different epochs is essential for accurate variability measurements. Taking into account potential zeropoint variations between different CCD chips and different exposures for a given epoch, we first run SCAMP to perform relative (internal) photometric calibration between different exposures so that the mean of the relative flux scaling parameter (FLXSCALE) is close to 1.0. Then we run SWarp (version 2.38.0; Bertin (2010)) with median mode to stack the individual exposures, and create a single-epoch image as well as the corresponding inverse variance weight map. The median stacking can further reject the residual cosmic rays. We run SExtractor to detect the bright objects in these single-epoch images and match the corresponding catalogs individually with the *Gaia* DR1 star catalog to generate the star samples for all epochs. The magnitudes of the stars are then restricted to be in the range of 17.5 mag to 21.5 mag. Quantitative comparison of the instrumental magnitudes of the common stars between any two different epochs shows that the median of the magnitude difference varies. For a few epochs, the difference can be even larger than 0.1 mag. This can be attributed to either the impact of different airmass or the non-photometric conditions. In this work, we do not distinguish these different effects and simply regard them as zeropoint variations. To eliminate such difference, we set the epoch with the best seeing in CDFS1 sub-field as reference, and scale the fluxes of other single-epoch images to the reference. The flux scaling factors are derived by comparing the instrumental fluxes of stars between the reference and other images. The partial overlap between the four sub-fields enables us to homogenize the zeropoints of all the single-epoch images to the reference. We find that the minimum overlap region between two adjacent sub-fields is about 110 arcmin<sup>2</sup>, resulting in ~150 common stars with good quality. According to the procedures, the final dispersion of the photometric calibration between different epochs is smaller than 0.02 mag.

### 2.1.3 Image Coaddition and Photometry

To assess the quality of each single-epoch image, we calculate the full width at half maximum (FWHM) and the elongation of stars, and the background fluctuation  $\sigma_{\text{bkg}}$ . We firstly exclude the epochs with median elongation larger than 0.1. The large elongation most probably results from the tracking instability of the telescope during the observation. The epochs with FWHM > 1.2'' and  $\sigma_{\text{bkg}} > 15.0$  ADUs are also rejected from the following analyses in order to reduce the object blending effect and positional uncertainty, as well as to optimize the signal-to-noise ratio (SNR) of objects. The excluded epochs have either large seeing or shallow limiting magnitude. Finally, we have 27, 21, 24 and 26 epochs for the CDFS1-4 sub-fields, respectively. Since the four sub-fields partially overlap with each other, the overlapping sky regions can have a larger number of observed epochs than the other regions. The very central sky region, covering about 1.7×6.2 arcmin<sup>2</sup> by the four sub-fields, has almost 98 observed epochs.

We then stack all the remaining single-epoch images using median combination method to create the final mosaic image (here-

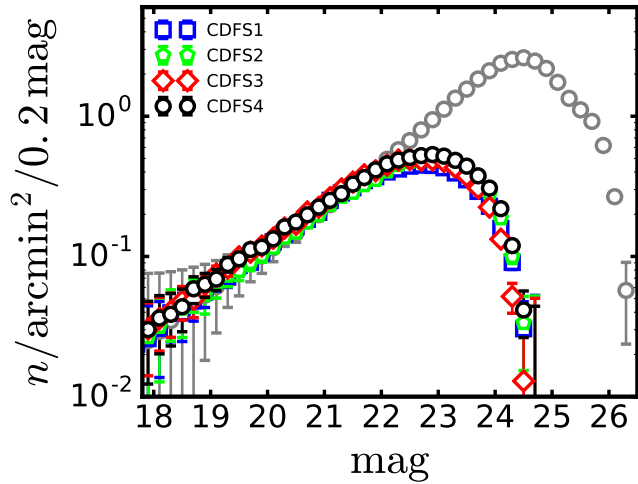


**Figure 1.** The  $r$ -band magnitude distributions with errorbars estimated from the Poisson statistics. The grey points represent the distribution of the *det* image, while the other four color-encoded distributions are the results by averaging the individual catalogs of all epochs for the sub-fields, respectively.

after *det* image). Again, the median coaddition enables us a further removal of residual cosmic rays, satellite tracks and other image defects remaining in the single-epoch image. In total, The *det* image covers  $4.38 \text{ deg}^2$  and it is used for objects detections and selections (see Section 3). The initial absolute photometric calibration was calculated by comparing the observed magnitudes of standard stars with photometric reference magnitudes. This was performed by the SUDARE-VOICE team based on the observation on July 30, 2012. In the present work, we directly compare the instrumental magnitudes of stars in the *det* image with the calibrated magnitudes to determine the final zeropoint and apply it to the individual epochs. The derived  $5\sigma$  limiting magnitude of the *det* image is about 26.3 mag for point source within  $1.0 \text{ arcsec}$  aperture radius.

Saturated stars and their surrounding halos can systematically affect the photometry on the nearby objects. We therefore visually identify all these regions and mask them from the *det* image. The area of such mask regions accounts for about 7 per cent of the original image.

We run SExtractor on the *det* image for object detection and photometry. The detection threshold is set to be  $2.0\sigma$  above the background, and at least three connected pixels are required for a detection. For photometry of the blended objects, we set the number of deblending threshold to be `DEBLEND_NTHRESH=32` and the low contrast parameter to be `DEBLEND_MINCONT=0.002`. In total, 381,937 objects are detected. The same configuration is also applied for the photometry on individual epochs. Figure 1 shows the  $r$ -band magnitude (`MAG_AUTO`) distributions of objects detected in the *det* image and the average of individual epochs for the four sub-fields. We can see that the peak of the magnitude distribution from the *det* image is about 24.5 mag which is close to the limiting magnitude of single epoch images.

## 2.2 PSF Modeling

For every epoch, we construct the spatially varied PSF model using PSFEx software (version 3.17.4; Bertin (2013)). Because each single-epoch image covers about  $1.0 \times 1.0 \text{ deg}^2$  and results from stacking single exposures, the spatial variations of the PSF over the

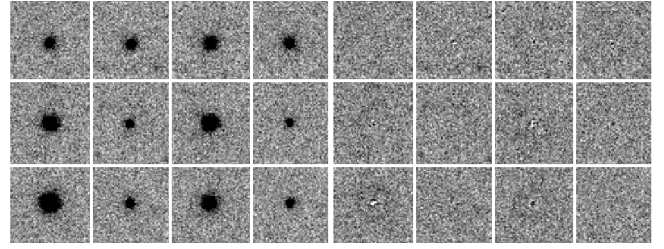


**Figure 2.** A typical example of PSF model constructed by PSFEx. The first four columns are star stamps selected for PSF modeling. While the last four columns show the corresponding residuals by subtracting the PSF models. The size of each stamp is  $12.2 \times 12.2 \text{ arcsec}^2$  with pixel scale of  $0.2 \text{ arcsec}$ .

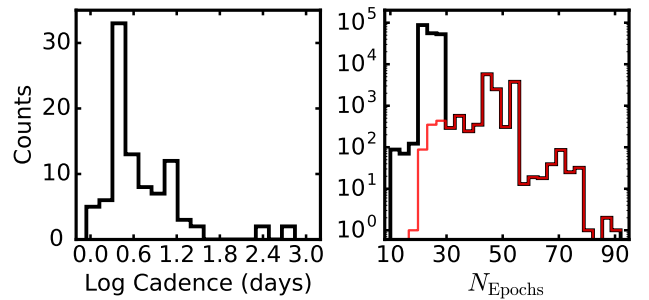


**Figure 3.** Histograms of the observed cadence and number of epochs for objects in the *clean* sample. The red line in the right figure represents the distribution of the epoch number for objects observed in at least two sub-fields.

entire image are significant (Fu et al. 2018). To accurately model the PSF variations with polynomial interpolation and reduce the impact of discontinuities at the CCD edges due to the stack of individual exposures, we firstly split the image into  $4 \times 2$  sub-images of uniform size. Basically, each sub-image covers the area of about  $2 \times 2$  CCD chips. The PSF model is then constructed for each sub-image individually.

To obtain a clean star sample for PSF modeling, we generate the object catalog for each sub-image and then match it with the *Gaia* DR1 catalog. Only unsaturated stars with SNR larger than 50 and SExtractor parameter `FLAGS=0` are selected. To reduce the non-linearity effect, stars with peak counts larger than half of the saturated values are also rejected. These criteria result in over 100 isolated and unsaturated stars for each sub-image as PSFEx input. We fix the image size of the PSF model (`PSF_SIZE`) to be  $31 \times 31$  pixels. To extract the principal components of the PSF model from Principal Component Analyses (PCAs), the basic vector parameter `BASIS_TYPE` is set to be `PIXEL`. A third-order polynomial function is applied to model the spatial variations. Finally, the PSF model at a given image position can be calculated by a linear combination of ten pixel basis vector images. Figure 2 displays a typical example to illustrate the accuracy of the PSF construction. Statistically comparing the stars with the corresponding PSF models shows that our implementation can yield near-zero model residuals. However, there still exist systematic biases in the very central region of the bright stars, as shown in Figure 2, which probably bias the photometry of the measured light curves. Therefore, we further perform the detrending correction on the light curves in the following section.

### 3 VARIABILITY MEASUREMENTS

In this section, we firstly describe the criteria to select objects for variability measurements. Then we introduce the drap method to extract the light curves for the selected objects, and present detailed error analyses on the results. It is noted that current time-domain surveys mainly focus on point-like objects (e.g. stars and quasars) or special extended objects (e.g. AGNs and SNe with observable hosts). In our studies here using drap, we do not make priori type selections. Thus the objects we analyze consist of both point-like and extended objects.

#### 3.1 Source Selection

The catalog extracted from the *det* image is used for initial object selection. As shown in Figure 1, most objects in the catalog are very faint and below the limiting depth of the individual epochs. Thus in our analyses, we conservatively select objects with SNR larger than 20.0 in the catalog, roughly corresponding to SNR $\sim$ 3.8 in a single epoch. This criterion rejects about 44.3% of the objects. We further exclude objects with *r*-band magnitude brighter than 16.0 mag which are basically saturated stars. Objects with bad photometry flagged by SExtractor are also rejected, but the blended pairs are allowed since they could be transient events (e.g. supernova and its host galaxy). In addition, objects with the total number of observed epochs less than 10 are removed. The selection criteria are summarized as follows:

- $r \geq 16.0$  mag & SNR  $\geq 20.0$
- FLAGS  $\leq 3$  (blending allowed)
- $n_{\text{epoch}} \geq 10$

Finally, 210,530 objects are selected for variability measurements, of which the faintest object reaches to  $r \sim 24.9$  mag. We refer to these objects as the *clean* sample. Figure 3 shows the histograms of the observational cadence and the number of epochs for objects in the sample. The peak cadence is about 3 days, and the fraction of objects which are observed in at least two sub-fields is about 7.0%.

For every object in the *clean* sample, we cut the stamps from all single-epoch images with a uniform size of 65 $\times$ 65 pixels, corresponding to 13 $\times$ 13 arcsec<sup>2</sup>. This size of stamp is about 11 times larger than the FWHM of the worst PSF (see Section 2.1.3). If the object is located at the edge (i.e. the distance between the center of the object and the edge of the image is less than 32 pixels) or inside a mask region in a certain epoch, that stamp is rejected. The PSF of an object is determined using the model constructed in Section 2.2 and is normalized so that the sum of its pixel values is equal to one.

#### 3.2 Differential Running-Average Photometry (DRAP)

In this subsection, we introduce the detailed mathematics on the drap method. For each object, the extracted stamps span many different photometric epochs. The background noise, the seeing conditions and the size and shape of the PSFs can vary between different epochs. For a given stamp *i*, the two dimensional surface brightness distribution of an object and the corresponding PSF profile are denoted as  $S_i$  and  $P_i$ , respectively. Then stacking all the stamps by weighted average method, we obtain a master stamp

$$S_0 = \sum_i^n w_i S_i / \sum_i w_i, \quad (1)$$

where  $w_i$  is the weight map of the stamp *i* and  $n$  is the total number of stamps. During the stack, the  $\sigma$ -clipping method is applied

to reject pixels with values (e.g. residual cosmic rays) larger than 5 times of the standard deviation. The outlier pixel values are replaced by the median of the surrounding 5 $\times$ 5 unmasked pixels. The same method is also used to stack the individual PSFs to yield the master PSF image, denoted as  $P_0$ . Similarly, excluding the *j*th stamp, then we can generate the stacked stamp  $\tilde{S}_j$  and corresponding PSF  $\tilde{P}_j$ . We can expect that the flux difference between the two stacked stamps  $S_0$  and  $\tilde{S}_j$  results from the variability of the object in the *j*th stamp. In addition, in Appendix A, we show that the two PSFs  $P_0$  and  $\tilde{P}_j$  are almost identical if  $n$  is much larger than the difference of the pixel values between  $P_j$  and  $P_0$ . The same conclusion also holds for the background fluctuations between the two stamps.

To illustrate the advantage of drap, for simplicity, assuming the PSF of each of our observational images is constant and follows the Gaussian profile with FWHM  $\mathcal{F}_{\text{epoch}}$  fixed to the observational value of the corresponding epoch, we calculate the FWHM  $\tilde{\mathcal{F}}$  of the running-average PSF for each epoch following the same procedure to obtain  $\tilde{P}_j$ . As shown in the top panel of Figure 4, while the PSF varies significantly for the individual epochs, the running-average PSF keeps very stable with maximum change of only 3.4% for CDFS2 sub-field. Similarly, the bottom panel of Figure 4 compares the background fluctuation  $\sigma_{\text{epoch}}$  of each epoch and the corresponding running-average value  $\tilde{\sigma}$  which is also very close to constant with maximum change of 6.1% for CDFS4 sub-field. The stable PSF and the background from drap make it very suitable for variability studies.

To measure the fluxes in the stacked stamps and precisely calculate the variability, we further perform PSF homogenization between the two stacked stamps although they are already rather stable. Different algorithms have been developed to construct the homogenization kernel, such as the deconvolution solution in Fourier space (Phillips & Davis 1995), regularization representation with a set of basis functions (Alard & Lupton 1998; Bramich 2008) and so forth. As discussed in Zackay et al. (2016), because of the effects of noise and other implementation issues, some homogenization operations can potentially lead to artifacts in the difference images. Here we homogenize the PSFs between the two stamps  $S_0$  and  $\tilde{S}_j$  using the cross-convolution method proposed by Gal-Yam et al. (2008). As noted there, this method can degrade both PSFs so that it may limit the detection of faint variable sources. However, since no deconvolution or regularization process is applied, it can be more numerically stable and leave less artifacts. In this case, the difference between the two stacked stamps is derived as

$$D_j = S_0 \otimes \tilde{P}_j - \tilde{S}_j \otimes P_0, \quad (2)$$

where  $\otimes$  represents the convolution operation.

We use aperture photometry to measure the residual flux, denoting as  $F_{D_j}$ , in the difference image  $D_j$ . For the variability measurements, we fix the aperture radius for all objects to be 1.5 arcsec which is about 1.26 times of the worst FWHM. With the convolution operation in the above equation, it is non-trivial to obtain the analytical expression between  $F_{D_j}$  and the true flux variation  $\delta F_j$  in the *j*th stamp. However, as mentioned above, in case of large  $n$ , we have  $P_0 \approx \tilde{P}_j$ . This approximation holds for all the current and future time-domain surveys which usually have hundreds of exposures on the same sky region (e.g. LSST (Ivezić et al. 2019)). In that case, the flux variation  $\delta F_j$  in the *j*th stamp relative to the flux in the master stamp can be simply derived as

$$\delta F_j = s \times F_{D_j}, \quad (3)$$

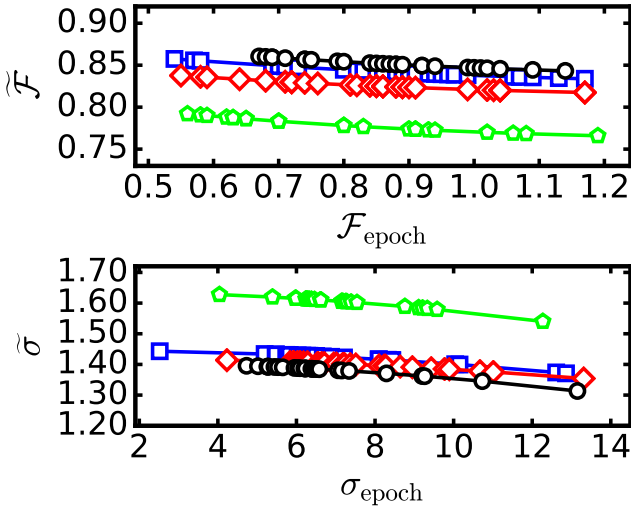


**Figure 4.** *Top panel:* comparison of the FWHM of PSF of each single epoch and the running-average result. Different colors, with the same notation as in Figure 1, corresponds to different sub-fields in SUDARE-VOICE survey. *Bottom panel:* comparison of the background fluctuation of each epoch and the running-average result.

where  $s$  represents the flux scaling factor which satisfies

$$Ns = \sum_{p,q} \sum_{i \neq j} w_i/w_j, \quad (4)$$

where  $N$  is the total number of pixels within the photometric aperture, and  $p$  and  $q$  are the pixel indices referring to the column and row of the weight map. The summation is performed within the photometric region. When the weights are identical,  $s$  reduces to  $s = n - 1$ . The corresponding flux error  $\sigma_{\delta F_j}$  is expressed as

$$\sigma_{\delta F_j} = s \times \sigma_{F_{D_j}} = s \times \sqrt{F_{D_j}/g + N\sigma_{\text{bkg}}^2}, \quad (5)$$

where  $g$  is the gain in the difference image, and  $\sigma_{\text{bkg}}$  is the rms of the background, which can be derived by  $n^2\sigma_{\text{bkg}}^2 = \sigma_j^2 + \tilde{\sigma}_j^2$  where  $\sigma_j$  and  $\tilde{\sigma}_j$  are the background fluctuations for  $S_j$  and  $\tilde{S}_j$ , respectively.

We generate a series of simulated image stamps of a star to validate the method. The light curve of the star is assumed to be sinusoidal, following  $m(t) = A \sin(t) + m_0$  where  $m(t)$  is the magnitude at time  $t$ ,  $A$  is the amplitude and  $m_0$  is a constant magnitude. In the simulation, we fix  $m_0 = 20.0$  mag and  $A = 0.4$  mag. We generate in total 27 stamps which is the same as the number of epochs in CDFS1 sub-field. The simulated PSFs follow Gaussian profile with FWHMs fixed to the observational values of individual epochs in the CDFS1 sub-field. Meanwhile, the background fluctuation values are also from the CDFS1 sub-field. The black curve in the top panel of Figure 5 shows the light curve of the star. The black circles represent the input magnitudes in the simulation, while the magenta squares with errorbars are the measured values by the drap method described above. The difference between the input and measured magnitudes is shown in the bottom panel of Figure 5. We see that the difference is consistent with zero with  $\sigma_{\Delta \text{mag}} \sim 0.01$ , meaning that the drap method can accurately recover the true light curve of the simulated star.

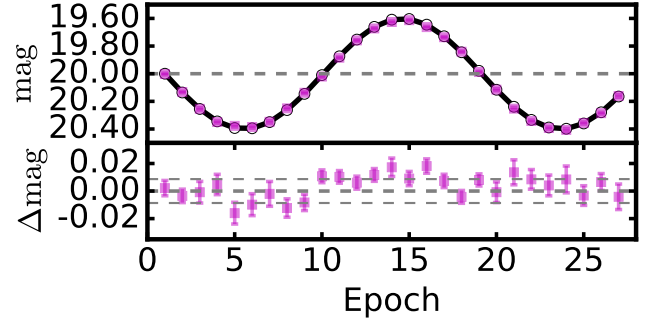


**Figure 5.** Comparison of the simulated light curve of a star and the measured result by the drap method. The light curve of the star is assumed to be sinusoidal, following  $m(t) = A \sin(t) + m_0$  where  $m(t)$  is the magnitude at time  $t$ ,  $A$  is the amplitude and  $m_0$  is a constant magnitude. In the simulation, we fix  $m_0 = 20.0$  mag and  $A = 0.4$  mag. *Top panel:* the black line is the light curve of the star. The black circles and the magenta squares with errorbars represent the input magnitudes in the simulation and the measured values by the drap method. *Bottom panel:* the magenta squares with errorbars represent the difference between the input and measured magnitudes. The thin dashed lines indicate the  $1.0\sigma$  dispersion of the magnitude difference.

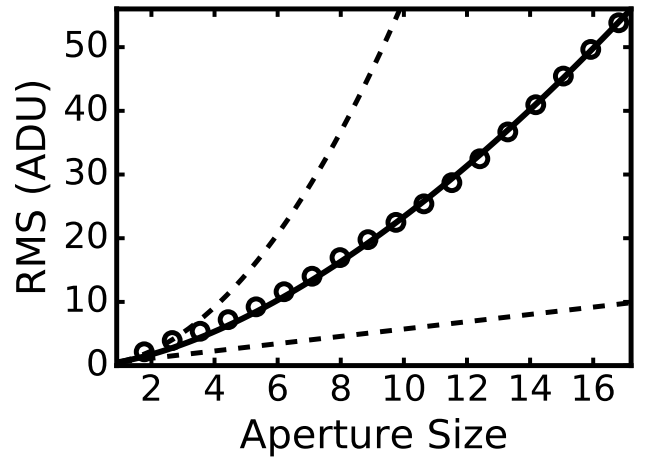


**Figure 6.** Gaussian dispersion as a function of aperture size defined as  $\sqrt{N}$ . The black circles are measured from the difference image  $D_j$ . A power-law curve with free parameter  $\beta$  (solid line) is used to fit the data points. For illustration, the bottom and top dashed curves represent two limiting cases: no pixel correlation and complete correlation in adjacent pixels.

### 3.3 Uncertainty Analyses

Since the image stacking and PSF convolution procedures can introduce correlated noise in the difference image  $D_j$ , Equation (5) may underestimate the uncertainty of the measured  $F_{D_j}$ . Without noise correlation, the background noise of a given image is determined by  $\sigma^2 = \sigma_0^2 N$ , where  $\sigma_0$  is the standard deviation of background noise and  $N$  is the pixel number in the photometric aperture. In the presence of noise correlation, however, the background noise should be estimated by  $\sigma^2 = \sigma_0^2 N^{2\beta}$ , where  $\beta$  is a free parameter within  $[0.5, 1.0]$ . In the case of pure background noise dominated,  $\beta = 0.5$ , while if the adjacent pixels are completely correlated,  $\beta = 1.0$  (Liu et al. 2017; Martínez-Palomera et al. 2018). Therefore, to take the noise correlation into account, the uncertainty of the measured  $F_{D_j}$  can be generalized as

$$\sigma_{F_{D_j}} = \sqrt{F_{D_j}/g + N^{2\beta}\sigma_{\text{bkg}}^2}. \quad (6)$$

We estimate the noise correlation as follows. For a given epoch, we obtain the corresponding running-average image  $\bar{I}$ . For simplicity, the PSF of the image  $\bar{I}$  is assumed to be Gaussian and spatially invariant. The size of the PSF is fixed to the value shown in Figure 4. Meanwhile, we can obtain the master image  $I$  and Gaussian PSF by average-stacking all the single epoch images. Then following the Equation (2) we can generate the difference image  $D_I$  for this epoch. To eliminate the potential impact of objects on estimating the noise, the positions in the difference image where objects are distinctly detected in the image  $I$  are masked. We then select a set of about 2000 random positions on the object-masked difference image. These positions are selected to be non-overlapping with the mask regions within radius of 20 pixels. The fluxes are measured for each position using different apertures. For a given aperture, a Gaussian function is used to fit the histogram of the measured fluxes to derive the dispersion. Generally, larger apertures give larger Gaussian dispersion. Then we use the power-law equation described above to fit the relation between Gaussian dispersion and aperture size as displayed in Figure 6 for an example. The derived  $\beta$  parameter, with value basically ranging from 0.6 to 0.8, is then applied to Equation (6) to revise the uncertainty.

### 3.4 Detrending

Although the PSFs between different stamps in the drap approach is rather stable, and we further perform PSF homogenization in the variability measurements, we still need a detrending procedure for calibration. Systematic biases on the measured light curves can be introduced for instance by a not accurate modeling of the positional variation of the PSF by a polynomial function, or by errors in the photometric calibrations of different epochs. Therefore, it is necessary to correct for these biases. Non-variable objects with constant fluxes as a function of time are ideal for such correction because any deviation of the measured flux at a given epoch from the expected value can be attributed to the systematic effects.

As with the PSF modeling, the detrending correction is performed, using the PSF stars as described in Section 2.2, on individual sub-images for a given epoch. The drap method is applied to measure the magnitudes of these stars. To eliminate the impact of variables, a star is rejected if the standard deviation of the magnitudes at all epochs larger than the  $3\sigma$  limit of the standard deviation of the whole sample as illustrated in Figure 12 (see Section 4 for more details). For each remaining star, we calculate the flux ratio  $s_j$  for the  $j$ th epoch relative to the flux measured on the master stamp  $S_0$ . Evidently, without the existence of systematic biases, the relative flux ratios of stars in a given sub-image should be equal to one. However, it is found that the relative flux ratios can be systematically as large as 5 per cents for some epochs (corresponding to the magnitude bias of about 0.06 mag). We apply a second order polynomial on each sub-image to model the systematic biases, and the detrending equation is written as

$$s_j(x, y) = p_0 + p_1x + p_2y + p_3x^2 + p_4xy + p_5y^2, \quad (7)$$

where  $p_i$  ( $i = 1, 2, \dots, 5$ ) are free parameters, and  $x$  and  $y$  are the pixel coordinates of stars in the sub-image. The least square fitting method is used to derive the best-fit parameters. The top panel of Figure 7 compares the light curves of a star before and after detrending correction. The shadow regions correspond to the standard deviations of the two light curves. After applying the detrending correction, the scatter of the light curve is decreased and well within the photometric accuracy. The similar result is also displayed for a

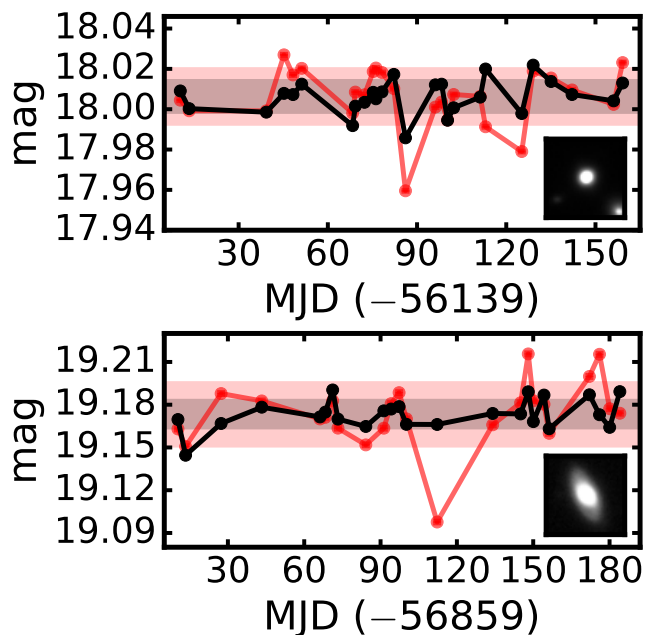


**Figure 7.** *Top panel:* Comparison between the light curves of a star before (red line) and after (black line) detrending correction. The shadow regions correspond to the  $1.0\sigma$  intervals around the mean magnitudes of the two light curves. The inset shows the stacked image stamp of the star. *Bottom panel:* Comparison between the light curves of a bright galaxy before (red line) and after (black line) detrending correction.

bright non-AGN galaxy in the bottom panel. We perform tests using higher order polynomial detrending. The results show no significant improvements comparing to the second order modeling.

Besides detrending, we also use median smoothing method to further reject the outliers due to bad photometry for a given light curve. The window size is set to be 5 consecutive data points. Then we subtract the smoothed light curve from the raw light curve. The residuals are expected to follow a Gaussian distribution with zero mean. In the presence of outliers, however, the standard deviation of the residuals derived by the usual method can be overestimated. Thus, instead, we calculate the median absolute deviation  $\sigma_{\text{mad}}$ <sup>3</sup> which is less sensitive to outliers (Bramich 2008) and is equal to the standard deviation for a Gaussian distribution. If the residual magnitude of a certain epoch is larger than  $5\sigma_{\text{mad}}$ , it is marked as an outlier. We note that this procedure may also potentially reject real variability, especially those explosive events with the time scale less than the cadence of our observations. However, they are beyond the reach using our data. The outlier removal method adopted here is therefore suitable for our analyses focusing on relatively long-time scale variables, such as AGN and SNe.

### 3.5 Comparison With Difference Imaging Method

Cappellaro et al. (2015) and Botticella et al. (2017) studied the SN explosion rates using the same dataset but only in the CDFS1-2 sub-fields. The SN candidates were detected by the difference imaging method *hotpants*<sup>4</sup> which is an implementation of the algorithm described in Alard & Lupton (1998). The PSF-fit photometry was

<sup>3</sup> The median absolute deviation is defined in this work as  $\sigma_{\text{mad}} = 1.483 \times \text{median}|x - \text{median}(x)|$ , where  $x$  is the data series.

<sup>4</sup> <https://github.com/acbecker/hotpants>



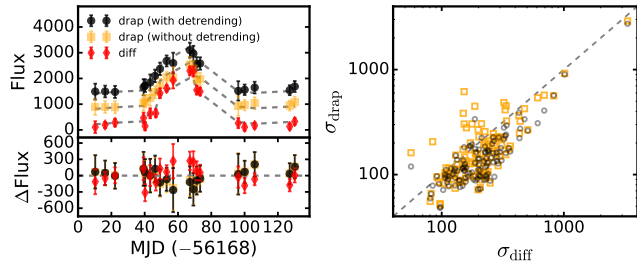


**Figure 8.** *Top left panel:* Comparison between the light curves measured by the difference imaging method and drap. The flux is in unit of analog-to-digital units (ADUs). The black dots (orange squares) represent the light curve measured by drap with (without) detrending correction. The red diamonds are the light curve measured by the difference imaging method hotpants. Arbitrary offsets are applied to the two light curves of drap for clarity. The dashed grey lines represent the intermediate light curve (see text for detail). *Bottom left panel:* Residuals after subtracting the intermediate light curve. *Right panel:* Comparison between the standard deviations of the light curve residuals of the two methods. The black dots represent the comparison to drap with detrending correction, while the orange squares without detrending correction.

then performed in the difference images to extract the light curves of these candidates. In this subsection, we compare the light curves measured by the difference imaging method and drap.

Through matching the SN sample with our *clean* sample, totally 116 common objects are acquired. The top left panel of Figure 8 compares the light curves of one SN candidate measured by the two methods. As expected, visual inspection shows that the light curves of all these common objects exhibit the same peak structures. To further check the photometric accuracy, for each object we average the detrended light curve of drap and the corresponding one measured by the difference imaging method, and then derive an intermediate light curve by applying the median smoothing method to the average. The dashed gray curves in the top left panel of Figure 8 shows the obtained intermediate light curve for this SN candidate, with the offsets between different lines the same as those for the data points. We subtract the intermediate light curve from the original light curves, as shown in the bottom left panel of Figure 8. The standard deviations ( $\sigma_{\text{diff}}$  and  $\sigma_{\text{drap}}$ ) of the residuals are calculated to quantify the photometric accuracy. The right panel of Figure 8 compare the results for all the 116 common objects. The dashed grey line corresponds to the one-to-one relation. It can be seen that the standard deviations measured by the difference imaging method are systematically larger than those of drap. Several reasons can be responsible for the results. Firstly, to perform image difference, the reference and new images used by Cappellaro et al. (2015) are both from single epoch observations which suffer from larger background and Poisson noises compared to drap. The differencing operation enlarges the noise level in the difference image, and hence leads to significant photometric uncertainty in the measured fluxes. Secondly, inaccurate modeling of the spatially varied PSF kernels in the difference imaging algorithm can not only lead to false positives in the difference image (Sánchez et al. 2019), but also affect the flux measurements of those real transients. Instead, the drap method can reduce the difference of PSFs between different epochs. In short, the reduced sensitivity to PSF variations and the reduced noise in drap comparing to those of hotpants leads to better light curve determinations with less dispersions of the data points around the resulting intermediate light curve.

## 4 RESULTS

The CDFS field has also been targeted by a number of photometric surveys, such as the *GALEX* ultraviolet survey (Martin et al. 2005), the Dark Energy Survey (DES; Dark Energy Survey Collaboration et al. (2016)), the deep Hyper Suprime-Cam survey (HSC, Ni et al. (2019)), the Pan-STARRS1 optical survey, the VIDEO near-infrared survey (Jarvis et al. 2013), the Spitzer SERVS and SWIRE mid/far-infrared surveys (Mauduit et al. 2012; Lonsdale et al. 2003), the HerMES submillimeter survey (Oliver et al. 2012) and the ATLAS radio survey (Norris et al. 2006; Franzen et al. 2015), producing a wealth of imaging data with large wavelength coverage. Spectroscopic observations in the field includes the 2dF Galaxy Redshift Survey (Colless et al. 2001), the 6dF Galaxy Survey (Jones et al. 2004, 2009), VVDS “Deep” survey (Le Fèvre et al. 2005, 2013), the VANDELS survey (Pentericci et al. 2018), the VUDS survey (Tasca et al. 2017), and the ongoing DEVILS survey (Davies et al. 2018). The central region of the field was also observed by a series of deep Chandra and XMM-Newton X-ray surveys (Luo et al. 2017; Xue et al. 2016; Comastri et al. 2011), and the CANDELS survey (Grogin et al. 2011; Koekemoer et al. 2011). A number of time-domain surveys and data, such as the *Catalina* real-time transient survey (Drake et al. 2009), the *SkyMapper* transient survey (Scalzo et al. 2017), the *Gaia* variable star catalog (Holl et al. 2018), the Pan-STARRS1 variable source catalog (Hernitschek et al. 2016), the Dark Energy Survey Supernova Program (DES-SN; Brout et al. (2019)), and the SUDARE-VOICE variability-selected AGN sample (Falocco et al. 2015; Poulain et al. 2020) etc., are also publicly available in this field.

The multi-band surveys and samples offer crucial datasets to study the physical properties of the variables and the host galaxies of transients. Because of the small sky coverage of the SUDARE-VOICE survey and limited number of objects in the *clean* sample, it is possible for us to visually inspect all the light curves. Quantitatively, we firstly calculate the average magnitude and the standard deviation  $\sigma$  of each light curve. One object is identified as variable if at least three sequential epochs deviate from the  $3\sigma$  region of the average magnitude. In total, we select 207 objects with significant variations. It is found that almost 80% of them display AGN-like light curves with aperiodic magnitude variations. Besides, we identify 44 transients, each of which shows significant single peak and dramatic magnitude change in the light curve. To demonstrate the effectiveness of the drap method, we show some examples in this section. More detailed analyses of the objects in combination with other multi-band data will be presented in our follow-up work.

We match the *clean* sample with the Million Quasars (MILLIQUAS) catalogue (v6.1<sup>5</sup>; Flesch (2015)) using a radius of 1.0 arc-second, obtaining 366 AGNs in total. Figure 9 shows the light curves of three confirmed AGNs<sup>6</sup> with different brightness and redshifts (top panel) and three AGN candidates (bottom panel) selected by our visual inspection. The AGN (ID #187389 in the *clean* sample) in the middle of top panel has observations in total 76 epochs spanning about three years. The AGN candidate (ID #198895) in the right of bottom panel, with SNR of 46.0 in the mosaic image, presents significant magnitude variations which is as large as about 1.2 mag. Meanwhile, we also show the light curves of the 44 transients in Figure 10. The orange triangles represent the magnitudes

<sup>5</sup> <http://www.quasars.org/milliquas.htm>

<sup>6</sup> The three AGNs are labeled as *Descr*=Q in the Million Quasars (MILLIQUAS) catalogue, meaning that they are type-I broad-line core-dominated quasars.

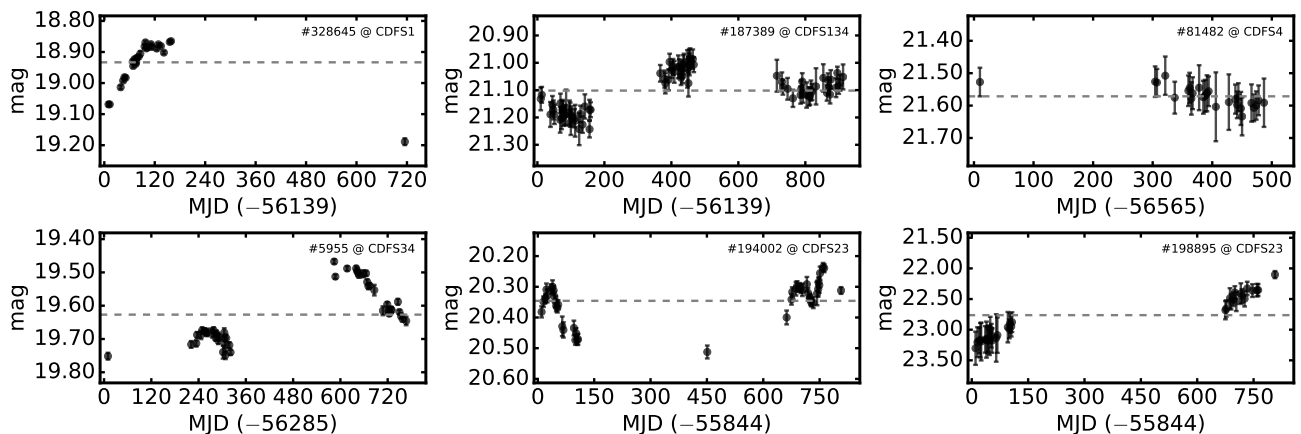


**Figure 9.** Light curves of AGNs and AGN candidates. Top panel shows three confirmed AGNs from the Million Quasar Catalog at different redshifts (from left to right the redshift is  $z = 1.025, 2.164, 3.872$ , respectively). The gray dashed line in each figure represents the magnitude measured in  $S_0$ , while the number is the ID in the *clean* sample. The bottom panel gives three AGN candidates which are not spectroscopically confirmed by any current survey.

below the  $5\sigma$  detection limit of point source. Figure 11 shows the corresponding image stamps generated by average-stacking all the available epochs, as well as the difference images of these transients at their peak brightness. It can be seen that most of the transients show relatively complete light curves from the starting of the event to fading. A large fraction of them are expected to be supernovae. To confirm that, we match these transients with the supernova sample detected in the CDFS1-2 sub-fields which used the same dataset (Cappellaro et al. 2015). For the 22 transients identified in the two sub-fields, only 6 transients (ID#197293, #286996, #291254, #297290, #308697 and #367376) are not classified as supernova by Cappellaro et al. (2015), of which the transient #197293 only detected during the observation of CDFS4 sub-field. Among the 44 transients, the one #158324 shows the largest magnitude variation of about 3.0 mag although we missed the observation of its peak. For this transient, we do detect its host galaxy in the HSC deep image (the observation was taken between January 2015 and March 2017 after the explosion) with  $r$ -band magnitude of 25.34 mag which is very faint but still consistent with our measurement as shown in the light curve. However, there are no near-infrared detections in the VIDEO  $JK_s$  bands (the limiting magnitudes for the two bands are 23.98 mag and 22.79 mag, respectively). Since there is no spectroscopic observation during the explosion and it now has disappeared in the sky, it will be challenging to classify this transient and investigate its properties into much detail.

Figure 12 shows the standard deviation  $\sigma$  and average magnitude of each light curve in the entire *clean* sample. The orange squares show the AGNs from the Million Quasar Catalog (Flesch 2015), and the magenta stars represent the 44 transients identified by visual inspection. The running median of the individual  $\sigma_i$  and its standard deviation  $\sigma_{[\sigma_i]}$  are calculated in a given magnitude bin with width of 0.5 mag. The dashed cyan line represents the  $3.0\sigma_{[\sigma_i]}$  threshold. It can be seen that one transient is below the threshold because only the transients with large magnitude variations tend to be selected by our visual inspection. For the AGN sample, however, we find that most of them fainter than 22.0 mag are below the threshold, meaning that the intrinsic dispersions of their light curves are comparable to the overall measured uncertainties. Further investigation indicates that most of them (72.4%) are X-ray detected AGNs (Wang et al. 2016). While the X-ray detected AGNs with magnitude brighter than 22.0 mag only account for 21.5%.

This result indicates that a fraction of AGNs could be missed out by only variability-selected method, as discussed in previous works of the SUDARE-VOICE collaboration (De Cicco et al. 2015; Falocco et al. 2015; De Cicco et al. 2019; Poulain et al. 2020).

## 5 SUMMARY

In this work, we use the SUDARE-VOICE  $r$ -band imaging data to extract the light curves of the detected objects in CDFS field. The total on-sky time for this field spans over four years, distributed over four adjacent sub-fields CDFS1-4. The multi-epoch  $r$ -band observations were taken with a cadence of about 3-4 days, avoiding the ten days around the full moon. Besides, this field has also been covered by many multi-band surveys, such as the GALEX survey, the DES, the deep HSC survey, the Pan-STARRS1 survey, the VIDEO survey and other infrared/radio surveys. The abundant datasets provide crucial information for studying the properties of the astronomical objects in this sky region.

To measure the light curves, careful image reduction are performed. We firstly stack the individual exposures for a given epoch to increase the SNR of the objects. The accuracy of the astrometric calibration reaches to 0.06 arcsec along both right ascension and declination axes. Then we photometrically calibrate the zero-points between different epochs so that the final accuracy of the photometric calibration is better than 0.02 mag. These calibrated epochs are combined, after rejecting several epochs with poor observational conditions, for object detections. Finally, 210,530 objects with high SNR and photometric quality are selected for light curve extractions. In addition, unbiased photometry between different epochs requires accurate PSF modeling. Taking into account the significant spatial variations of the PSF, we split each epoch into  $4\times 2$  sub-images with uniform size, and construct the PSF model for each sub-image individually of which the spatial variation is described by polynomial interpolation.

For each object, the image stamps of all available epochs and corresponding PSF models are extracted. We introduce a new method, namely *drap*, to measure the light curves of these objects. The mathematics of this method is quite straightforward. It can moderately average out the difference of PSFs between different epochs, and suppress the background fluctuations. We estimate the photometric uncertainty of the light curves by taking the noise

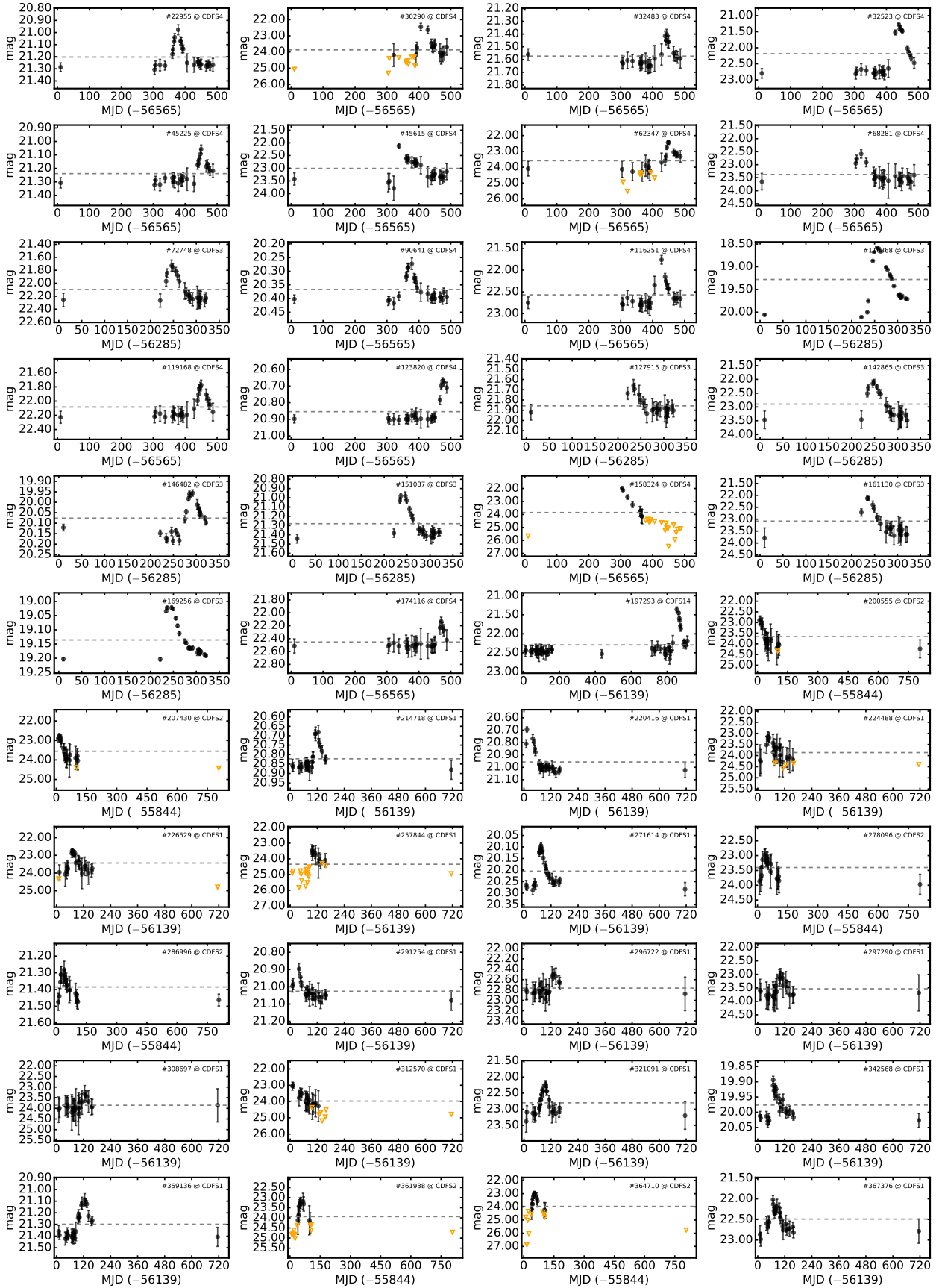


**Figure 10.** Light curves of the transients identified by visual inspection. The orange triangles are measures below the  $5\sigma$  limiting magnitude. The labels are the same as in Figure 9.

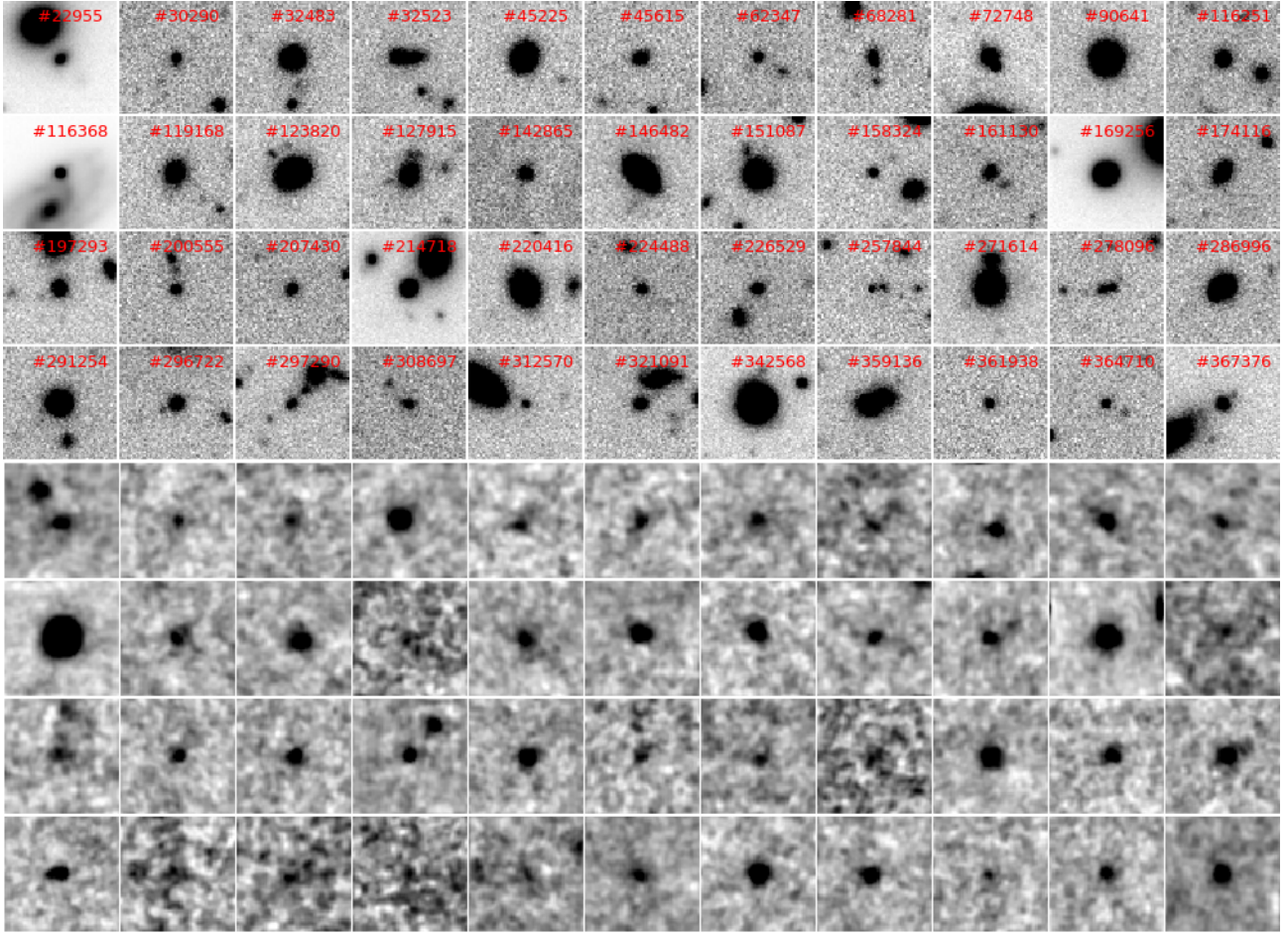


**Figure 11.** *Top four panels:* The  $r$ -band image stamps of the transients and their host galaxies. These stamps are generated by average-stacking all the epochs. The size of each stamp is  $65 \times 65$  pixels, corresponding to  $13 \times 13$  arcsec<sup>2</sup>. The attached number represents the ID in the *clean* sample. *Bottom four panels:* The corresponding difference images of the transients at their peak brightness.

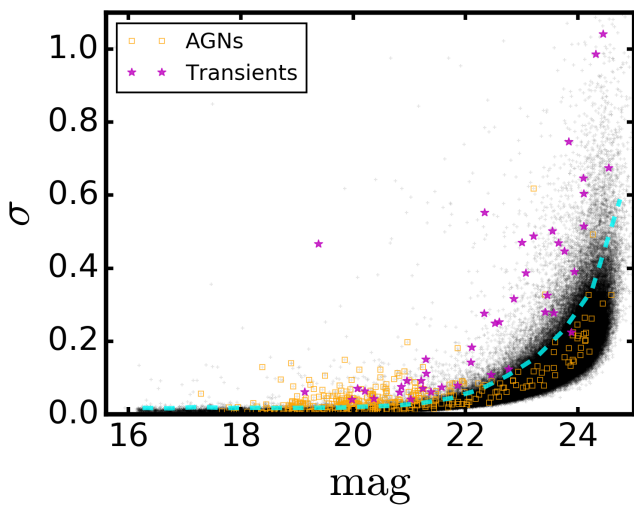


**Figure 12.** The standard deviation as a function of average magnitude for the entire sample (black crosses). The orange squares show the AGNs from the Million Quasar Catalog, and the magenta stars represent the transients identified by visual inspection. The dashed cyan line is the  $3.0\sigma_{[\sigma_i]}$  threshold of the standard deviation.

correlation into consideration, and perform detrending correction to eliminate the systematic biases due to the inaccurate image reduction and PSF modeling. We visually inspect the light curves to select variable objects. As expected, most of the variable objects are AGNs with aperiodic and long-term magnitude variations. We identify 44 transients with significant magnitude variations. For the 22 transients in CDFS1-2 fields, 16 of them are classified as supernova by Cappellaro et al. (2015), meaning that most of the transients we identified are supernovae. We will perform further studies on these objects in combination with multi-band data in the follow-up work.

**ACKNOWLEDGEMENTS**

DZL thanks Zhenya Zheng and Chenggang Shu for their helpful discussions and comments. This work is supported by the Launching Research Fund for Postdoctoral Fellow from the Yunnan University with grant C176220200 and the China Postdoctoral Science Foundation with Grant No. 2019M663582. ZHF acknowledges the support of National Nature Science Foundation of China (NSFC) under the grants 11933002, 11333001, and 11653001. LPF acknowledges the support from NSFC grants 11722326, 11673018 & 11933002, STCSM grant 18590780100,

19590780100, 188014066, the Innovation Program 2019-01-07-00-02-E00032 and Shuguang Program 19SG41 supported by SMEC. GC acknowledges the SWIFAR visiting fellow program under which he had a fruitful visit to the South-Western Institute for Astronomy Research, Yunnan University. MV and LM acknowledge support from the Italian Ministry of Foreign Affairs and International Cooperation (MAECI Grant Number ZA18GR02) and the South African Department of Science and Technology's National Research Foundation (DST-NRF Grant Number 113121) as part of the ISARP RADIOSKY2020 Joint Research Scheme. Support for G.P. is provided by the Ministry of Economy, Development, and Tourism's Millennium Science Initiative through grant IC120009, awarded MAS.

This work has made use of data from the European Space Agency (ESA) mission *Gaia* (<https://www.cosmos.esa.int/gaia>), processed by the *Gaia* Data Processing and Analysis Consortium (DPAC, <https://www.cosmos.esa.int/web/gaia/dpac/consortium>). Funding for the DPAC has been provided by national institutions, in particular the institutions participating in the *Gaia* Multilateral Agreement.

## REFERENCES

- Abbott, T. M. C., Allam, S., Andersen, P., et al. 2019, *ApJ*, 872, L30
- Alard, C., & Lupton, R. H. 1998, *ApJ*, 503, 325
- Astier, P., Guy, J., Regnault, N., et al. 2006, *A&A*, 447, 31
- Benedict, G. F., McArthur, B. E., Feast, M. W., et al. 2007, *AJ*, 133, 1810
- Bertin, E., & Arnouts, S. 1996, *A&AS*, 117, 393
- Bertin, E. 2006, *Astronomical Data Analysis Software and Systems XV*, 351, 112
- Bertin, E. 2010, *Astrophysics Source Code Library*, ascl:1010.068
- Bertin, E. 2013, *Astrophysics Source Code Library*, ascl:1301.001
- Botticella, M. T., Cappellaro, E., Greggio, L., et al. 2017, *A&A*, 598, A50
- Bramich, D. M. 2008, *MNRAS*, 386, L77
- Brammer, G. B., van Dokkum, P. G., & Coppi, P. 2008, *ApJ*, 686, 1503
- Brout, D., Sako, M., Scolnic, D., et al. 2019, *ApJ*, 874, 106
- Cappellaro, E., Botticella, M. T., Pignata, G., et al. 2015, *A&A*, 584, A62
- Catelan, M., & Smith, H. A. 2015, *Pulsating Stars* (Wiley-VCH)
- Colless, M., Dalton, G., Maddox, S., et al. 2001, *MNRAS*, 328, 1039
- Comastri, A., Ranalli, P., Iwasawa, K., et al. 2011, *A&A*, 526, L9
- Covone, G., de Ritis, R., Dominik, M., et al. 2000, *A&A*, 357, 816
- Dark Energy Survey Collaboration, Abbott, T., Abdalla, F. B., et al. 2016, *MNRAS*, 460, 1270
- Davies, L. J. M., Robotham, A. S. G., Driver, S. P., et al. 2018, *MNRAS*, 480, 768
- De Cicco, D., Paolillo, M., Covone, G., et al. 2015, *A&A*, 574, A112
- De Cicco, D., Paolillo, M., Falocco, S., et al. 2019, *A&A*, 627, A33
- Drake, A. J., Djorgovski, S. G., Mahabal, A., et al. 2009, *ApJ*, 696, 870
- Fabbro, S. 2001, PhD thesis, Université Denis Diderot, Paris
- Falocco, S., Paolillo, M., Covone, G., et al. 2015, *A&A*, 579, A115
- Flesch, E. W. 2015, *Publ. Astron. Soc. Australia*, 32, e010
- Foreman-Mackey, D., Hogg, D. W., Lang, D., & Goodman, J. 2013, *PASP*, 125, 306
- Förster, F., Maureira, J. C., San Martín, J., et al. 2016, *ApJ*, 832, 155
- Franzen, T. M. O., Banfield, J. K., Hales, C. A., et al. 2015, *MNRAS*, 453, 4020
- Fu, L., Liu, D., Radovich, M., et al. 2018, *MNRAS*,
- Gal-Yam, A., Maoz, D., Guhathakurta, P., & Filippenko, A. V. 2008, *ApJ*, 680, 550
- Gaia Collaboration, Brown, A. G. A., Vallenari, A., et al. 2016, *A&A*, 595, A2
- Giacconi, R., Rosati, P., Tozzi, P., et al. 2001, *ApJ*, 551, 624
- Grado, A., Capaccioli, M., Limatola, L., & Getman, F. 2012, *Memorie della Societa Astronomica Italiana Supplementi*, 19, 362
- Graham, M. J., Kulkarni, S. R., Bellm, E. C., et al. 2019, *PASP*, 131, 078001
- Grogin, N. A., Kocevski, D. D., Faber, S. M., et al. 2011, *ApJS*, 197, 35
- Hernitschek, N., Schlafly, E. F., Sesar, B., et al. 2016, *ApJ*, 817, 73
- Holl, B., Audard, M., Nienartowicz, K., et al. 2018, *A&A*, 618, A30
- Ivezić, Ž., Kahn, S. M., Tyson, J. A., et al. 2019, *ApJ*, 873, 111
- Jarvis, M. J., Bonfield, D. G., Bruce, V. A., et al. 2013, *MNRAS*, 428, 1281
- Jones, D. H., Saunders, W., Colless, M., et al. 2004, *MNRAS*, 355, 747
- Jones, D. H., Read, M. A., Saunders, W., et al. 2009, *MNRAS*, 399, 683
- Kaiser, N. 2004, *Proc. SPIE*, 5489, 11
- Koekemoer, A. M., Faber, S. M., Ferguson, H. C., et al. 2011, *ApJS*, 197, 36
- Kuijken, K. 2011, *The Messenger*, 146, 8
- Law, N. M., Kulkarni, S. R., Dekany, R. G., et al. 2009, *PASP*, 121, 1395
- Lawrence, A. 2016, *Astronomical Surveys and Big Data*, 505, 107
- Le Fèvre, O., Vettolani, G., Garilli, B., et al. 2005, *A&A*, 439, 845
- Le Fèvre, O., Cassata, P., Cucciati, O., et al. 2013, *A&A*, 559, A14
- Liu, D., Yang, J., Yuan, S., et al. 2017, *AJ*, 153, 53
- Liu, D., Fu, L., Liu, X., et al. 2018, *MNRAS*, 478, 2388
- Lonsdale, C. J., Smith, H. E., Rowan-Robinson, M., et al. 2003, *PASP*, 115, 897
- Luo, B., Brandt, W. N., Xue, Y. Q., et al. 2017, *ApJS*, 228, 2
- Martin, D. C., Fanson, J., Schiminovich, D., et al. 2005, *ApJ*, 619, L1
- Martínez-Palomera, J., Förster, F., Protopapas, P., et al. 2018, *AJ*, 156, 186
- Mauduit, J.-C., Lacy, M., Farrah, D., et al. 2012, *PASP*, 124, 714
- Ni, Q., Timlin, J., Brandt, W. N., & Yang, G. 2019, *Research Notes of the American Astronomical Society*, 3, 5
- Norris, R. P., Afonso, J., Appleton, P. N., et al. 2006, *AJ*, 132, 2409
- Oelkers, R. J., Macri, L. M., Wang, L., et al. 2015, *AJ*, 149, 50
- Oliver, S., Rowan-Robinson, M., Alexander, D. M., et al. 2000, *MNRAS*, 316, 749
- Oliver, S. J., Bock, J., Altieri, B., et al. 2012, *MNRAS*, 424, 1614
- Pentericci, L., McLure, R. J., Garilli, B., et al. 2018, *A&A*, 616, A174
- Perlmutter, S., Aldering, G., Goldhaber, G., et al. 1999, *ApJ*, 517, 565
- Phillips, A. C., & Davis, L. E. 1995, *Astronomical Data Analysis Software and Systems IV*, 77, 297
- Poulain, M., Paolillo, M., De Cicco, D., et al. 2020, *arXiv e-prints*, arXiv:2001.02560
- Rich, J. A., Madore, B. F., Monson, A. J., et al. 2018, *ApJ*, 869, 82
- Riess, A. G., Filippenko, A. V., Challis, P., et al. 1998, *AJ*, 116, 1009
- Rowan-Robinson, M., Lari, C., Perez-Fournon, I., et al. 2004, *MNRAS*, 351, 1290
- Sánchez, P., Lira, P., Cartier, R., et al. 2017, *ApJ*, 849, 110
- Sánchez, B., Domínguez R., M. J., Lares, M., et al. 2019, *Astronomy and Computing*, 28, 100284
- Scalzo, R. A., Yuan, F., Childress, M. J., et al. 2017, *Publ. Astron. Soc. Australia*, 34, e030
- Stassun, K. G., Oelkers, R. J., Pepper, J., et al. 2018, *AJ*, 156, 102
- Strubbe, L. E., & Quataert, E. 2009, *MNRAS*, 400, 2070
- Tasca, L. A. M., Le Fèvre, O., Ribeiro, B., et al. 2017, *A&A*, 600, A110
- Thompson, S. E., Coughlin, J. L., Hoffman, K., et al. 2018, *ApJS*, 235, 38
- Tozzi, P., Rosati, P., Nonino, M., et al. 2001, *ApJ*, 562, 42
- Vaccari, M., Lari, C., Angeretti, L., et al. 2005, *MNRAS*, 358, 397
- Vaccari, M., Marchetti, L., Franceschini, A., et al. 2010, *A&A*, 518, L20
- Vaccari, M. 2015, *The Many Facets of Extragalactic Radio Surveys: Towards New Scientific Challenges*, 27
- Vaccari, M., Covone, G., Radovich, M., et al. 2016, *Proceedings of the 4th Annual Conference on High Energy Astrophysics in Southern Africa (HEASA 2016)*, 25-26 August, 26
- Vaccari, M. 2016, *The Universe of Digital Sky Surveys*, 71
- van Dokkum, P. G. 2001, *PASP*, 113, 1420
- Wang, S., Liu, J., Qiu, Y., et al. 2016, *ApJS*, 224, 40
- Wang, B., & Han, Z. 2012, *New Astron. Rev.*, 56, 122
- Xue, Y. Q., Luo, B., Brandt, W. N., et al. 2016, *ApJS*, 224, 15
- Zackay, B., Ofek, E. O., & Gal-Yam, A. 2016, *ApJ*, 830, 27

**APPENDIX A: MINIMIZING THE PSF VARIATIONS BY AVERAGE STACKING**

We stack the individual PSFs to derive the master PSF  $P_0$  by

$$P_0 = \sum_i^n P_i/n, \quad (A1)$$

where  $P_i$  is the PSF of the  $i$ th stamp and  $n$  is the total number of stamps. Similarly, excluding the PSF  $P_j$  of the  $j$ th stamp, then we can generate the stacked PSF  $\tilde{P}_j$ . It is noted that both the individual and stacked PSFs have been normalized so that the sum of all the pixels is equal to one. Since the stacking is performed pixel by pixel, for simplicity but without loss of generality, we can instead analyze the behavior of the stacked PSFs in an arbitrary pixel position  $(x, y)$ , where  $x$  and  $y$  represent the pixel indices of the two-dimensional PSF matrix. For a specified pixel position  $(p, q)$ , the intensities of the master PSF  $P_0$  and  $\tilde{P}_j$  can be calculated respectively by

$$P_0^{pq} = \sum_i^n P_i^{pq}/n \quad \text{and} \quad \tilde{P}_j^{pq} = \sum_{i \neq j}^n P_i^{pq}/(n-1), \quad (A2)$$

where  $P_i^{pq}$  is the intensity of the  $i$ th PSF at position  $(p, q)$ . Through simple mathematical transformation, we can find that  $P_0^{pq}$  and  $\tilde{P}_j^{pq}$  satisfies

$$nP_0^{pq} = (n-1)\tilde{P}_j^{pq} + P_j^{pq}, \quad (A3)$$

namely,

$$P_0^{pq} - \tilde{P}_j^{pq} = \frac{P_j^{pq} - P_0^{pq}}{n-1}. \quad (A4)$$

It proves that the two PSFs  $P_0$  and  $\tilde{P}_j$  are almost identical if  $n$  is much larger than the difference of the pixel values between  $P_j$  and  $P_0$ . For the VOICE data, the mean difference of the central values between the normalized  $P_j$  and  $P_0$  is 0.03, meaning that  $|P_0^{pq} - \tilde{P}_j^{pq}| \lesssim 10^{-3}$  when  $n \simeq 20$ .